

Effect of Slot-Guidance and Slot-Area on Air Entrainment in a Conical Ejector Diffuser for Infrared Suppression

L. Singh, S. N. Singh[†] and S. S. Sinha

Department of Applied Mechanics, Indian Institute of Technology Delhi, New Delhi, 110016, India

[†]Corresponding Author Email: sns@am.iitd.ac.in

(Received June 26, 2018; accepted December 5, 2018)

ABSTRACT

A numerical study has been carried out on a new design of ejector diffuser (infrared suppression device). New design conceptualizes exploiting the shape of the slot openings. A circular arc is provided to guide the entrained fluid at the slot openings. Performance of guided-slot ejector diffuser (GED) has been compared with conventional (non-guided-slot) ejector diffuser (NGED) in terms of local and cumulative mass entrainment ratios, temperature distribution and static pressure recovery. Three slot-area variations are also studied, namely (i) increasing slot-area ranging $1 \leq A_0 \leq 2.02$, (A_0 is area of 1st slot) (ii) constant slot-area $A_0 = 1$ and (iii) decreasing slot-area ranging $0.49 \leq A_0 \leq 1$. Simulations have been carried out at fixed Reynolds number $Re = 1.3 \times 10^5$. It is observed that GED has 3.5% higher cumulative mass entrainment ratio than NGED. GED forms cold annulus region below ejector diffuser wall from 1st slot onwards which results in wall temperatures being close to ambient temperature (300 ° K). Higher mass entrainment rate and lower wall temperatures make GED a better infrared suppression device but static pressure recovery is better in NGED ($C_p = 0.79$) compared to GED ($C_p = 0.43$). Slot-area study reveals that the performance of increasing slot-area for GED and NGED is superior than constant and decreasing slot-area configurations. The cumulative mass entrainment is 20% higher while static pressure recovery is 45% more for the increasing slot-area GED when compared to the decreasing slot-area GED.

Keywords: Mass entrainment; Slot openings; Heat signatures; Static pressure recovery; Numerical study.

NOMENCLATURE

A_0	area of 1 st slot	m_{je}	entrained mass flow rate through opening
AR_{df}	diffuser exit to inlet area ratio	p_{ex}	mass weighted averaged static pressure at exit
AR_{mx}	mixing tube to nozzle exit area ratio	p_{in}	mass weighted averaged static pressure at inlet
C_p	coefficient of static pressure recovery	q	inlet dynamic pressure
D_{mx}	mixing tube diameter	Re_{nz}	nozzle exit Reynolds number
D_{nz}	nozzle exit diameter	SD	standoff distance
D_{pl}	diameter of plenum	T_0	ambient temperature
L_{df}	length of diffuser	T_g	temperature of exhaust gas at the nozzle exit
L_{mx}	mixing tube length		
L_{nz}	nozzle length		
L_{pl}	length of plenum		
L_{sd}	length of standoff distance	κ	local mass entrainment ratio
L_{tp}	length of tail pipe	ϕ	cumulative mass entrainment ratio
m_{in}	nozzle exit mass flow rate	ψ	normalized temperature variation

1. INTRODUCTION

Helicopters, ships and other such vehicles operating inside enemy lines are vulnerable to infrared (IR) homing missiles as these can intercept targets by sensing their IR energy (Rao and Mahulikar, 2002). It works on the principle of discriminating IR radiance of the target from the background. Its use is limited to specific bands in the IR spectrum such as 3-5 μm and 8-12 μm (Birk and VanDam, 1989). The threat of IR sensing missiles on vehicles is reduced by utilizing IR suppression system (IRSS). Ejector diffuser is a passive IRSS device (Birk and VanDam, 1989) and forms the exhaust assembly of a gas turbine (GT) engine. Exhaust gases from GT engine flow through ejector diffuser and exit into the atmosphere. As an IRSS device, it is highly desirable for an ejector diffuser to lower the exhaust gases temperature before exiting into the atmosphere. Thus ejector-diffuser are designed with the ability to bring down the temperature of exhaust gases by entraining low-temperature ambient air and its mixing with the exhaust gases within the ejector diffuser.

Ejector diffuser consists of three main components namely (i) nozzle, (ii) mixing tube and (iii) diffuser as shown in Figure 1. Nozzle and mixing tube is commonly referred as ejector. Exhaust gases from GT engine leave nozzle as a jet, and enters into the mixing tube. Mixing tube may or may not be attached to the nozzle. If a gap exists between nozzle and mixing tube, it is referred as standoff-distance (SD). Mixing tube has a uniform cross-section throughout its length. At the end of mixing tube, a diffuser is attached. The diffuser has an increasing cross-sectional area, and it has slot openings along the periphery at different axial lengths. The slots could be a step-slot as shown in Fig. 1 or these could be in line with the diffuser wall (Fig. 2).

Entrainment of low-temperature atmospheric air happens through peripheral openings of the ejector diffuser. The peripheral openings are of two types (i) standoff distance (SD) and (ii) slots. The slots are strategically placed as steps or in-line openings on diffuser surface. While SD is characterized by its length and area ratio (mixing tube to nozzle exit), slots are characterized by slot area and slot shape. SD and slots form essential design parameters for ejector diffuser performance.

Performance of ejector diffuser is gauged by local mass entrainment, cumulative mass entrainment, mixing of entrained air with the hot exhaust gases to lower the exhaust temperatures and static pressure recovery. Beside SD and slot, other geometrical parameters include mixing tube length, diffuser area ratio and diffuser cone angle. Flow dynamical parameters include nozzle exit Reynolds number (Renz), inlet boundary layer, nozzle exit velocity profile, nozzle exit turbulence intensity, swirl, etc.

Barik *et al.* (2015) conducted experimental study on the effect of Re_{nz} ($3525 < Re_{nz} < 7073$) on mass entrainment for an ejector diffuser. They found that mass entrainment rate increases linearly with increase in Reynolds number and is function of

Reynolds number for the range investigated. Singh *et al.* (2009) conducted experimental study on non-circular ejector diffuser at three Reynolds number $Re_{nz} = 2 \times 10^5, 2.5 \times 10^5, 3 \times 10^5$. They found that mass entrainment rate is identical in three cases which indicates that performance of ejector diffuser is independent of Reynolds number when $Re_{nz} > 2 \times 10^5$. Similar finding has been reported by Sen (2008). However in case of standalone ejectors, mass entrainment rate is independent of Reynolds number when $Re_{nz} > 2 \times 10^4$ (Vyas and Kar 1975; Reneau *et al.* 1967; Carletti *et al.* 1995). Literature survey shows that the performance of ejector diffuser (similar type) becomes Reynolds number independent beyond or equal to 10^5 . In the current study investigation has been conducted at a fixed $Re_{nz} = 1.3 \times 10^5$.

Diffuser inlet conditions such as inlet velocity profile, turbulence intensity, and swirl affect the performance of diffuser mainly concerning static pressure recovery coefficient (C_p). The diffuser inlet velocity profile is often correlated with inlet flow blockage parameter (Waitman *et al.* 1961; Henry and Wilbur, 1956). Blockage parameter is the ratio of displacement thickness to inlet width. Diffuser performance is affected much more by inlet blockage factor than flow regime, and thus performance decreases with increase in blockage factor (Reneau *et al.* 1967). Presence of thinnest boundary layer at diffuser inlet limits C_p to less than 0.9, whereas the higher value of turbulence intensity at diffuser inlet has resulted in improved C_p in the case of large area ratio diffusers (Klein, 1981). Increase in turbulent intensity from 0.48% to 4.97% for a two-dimensional diffuser with a cone angle of 20° showed an increase in pressure recovery by 20% (Hoffmann and Gonzalez, 1984). In addition swirl, defined as the ratio of angular to axial momentum, at diffuser inlet affects C_p .

Experimental study on the effect of swirl on conical diffusers was carried out by Fox and McDonald (1971) and Senoo *et al.* (1978). They found that in the case of the wide-angle diffuser (cone angle of 20°), moderate swirl number improves C_p by 36%.

However at high swirl numbers C_p value drops. In the ejector diffuser design, the diffuser is attached to the mixing tube which makes it immune to any alteration from outside, and diffuser inlet conditions are solely dependent on mixing tube exit conditions. No specific inputs are applied at diffuser inlet to influence the performance.

Nozzle exit shape affects flow characteristics which in turn influence mass entrainment rate and mixing properties by an ejector. Skebe *et al.* (1988) carried out experimental work on lobbed and circular nozzle while varying mixing tube length. They reported an increase in the mass entrainment rate by 200% and also achieved mixing of entrained fluid with core within half the length of original mixing tube. Hu *et*

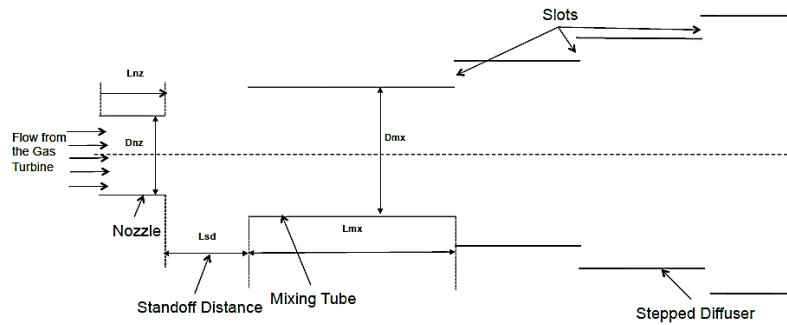


Fig. 1. Components of ejector diffuser.

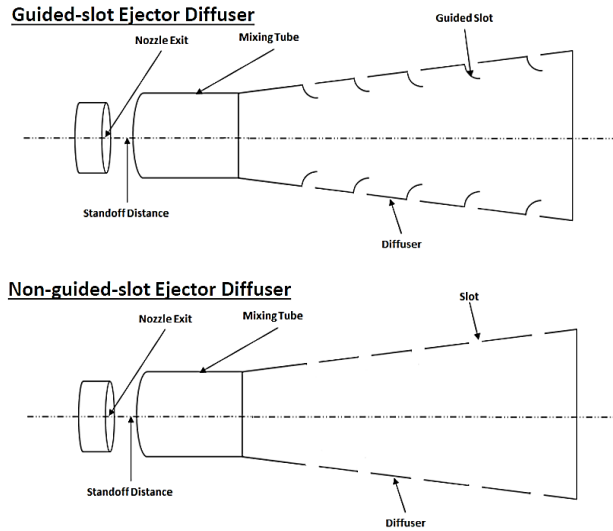


Fig. 2. Geometric outline for guided-slot and non-guided-slot ejector diffuser.

al. (1996) conducted an experimental study on the rectangular lobbed nozzle and reported an increase in mass entrainment rate by 300% over the circular nozzle. In another study by *Hu et al.* (2000), it is reported that lobbed nozzle offers improved mixing wherein the potential core length reduces by 16% indicating early interaction of the entrained fluid with exhaust jet core. *Mohammadaliha et al.* (2016) studied three nozzle shapes (circular, square, rectangular) and found an increase in mass entrainment of around 8% for the square nozzle compared to circular nozzle. No advantage in mass entrainment was observed by changing the aspect ratio (upto 4) of the rectangular nozzle. However, the present study evaluates the ejector diffuser performance for a circular nozzle shape only.

Studies have been reported where optimum values of the length of Standoff distance (L_{sd}) and mixing tube to nozzle exit area ratio (AR_{mx}) are suggested for best performance of ejector. *Mitchell and London* (1958) carried out experimental study on straight circular air-air ejector and reported $L_{sd} = 1.35D_{nz}$, D_{nz} is diameter of nozzle exit, and $AR_{mx} = 1.835$ as optimum values. Similar studies by *Mueller* (1964), *Silvester and Mueller* (1968), *Reddy and Kar* (1968) and *Bonnington and King* (1972) reported optimal value to exist in the range $0.8D_{nz} < L_{sd} < 2D_{nz}$. Recently, a numerical study by *Singh et al.* (2017)

have reported $L_{sd} = 2.25D_{nz}$ and $AR_{mx} = 2.25$ as optimum values for air-air circular ejector. *Sen* (2008) work on circular ejector diffuser reported optimum range for L_{sd} as $2D_{nz} < L_{sd} < 3D_{nz}$.

Ejector diffuser finds application in combat vehicles pertaining to defense industry, hence limited open literature is available. Few studies on ejector diffuser have been reported in the past decade. These studies were carried out keeping combat vehicles in mind. *Sen* (2008) carried out work in stepped slot conical ejector diffuser. They reported that the length of overlap for two concentric tubes at a given step slot does not influence the performance. But increase in interface height (thickness of diffuser wall) adversely affects the performance of ejector diffuser. Slot geometry in terms of inclined slot opening was also studied. Single-side inclined case showed better mass entrainment rate than a both-side inclined case. Effect of swirl showed a drop in the mass entrainment rate for moderate swirl number. *Singh et al.* (2009) conducted experimental study on rectangular shaped ejector diffuser with focus on diffuser area ratio. They reported that mass entrainment rate drops by 24% when diffuser area ratio is increased from 9 to 25. Another study by *Singh et al.* (2013) reports that increasing the number of slot openings from 5 to 10 while keeping other geometrical parameters as same, the cumulative mass entrainment rate was found to be independent

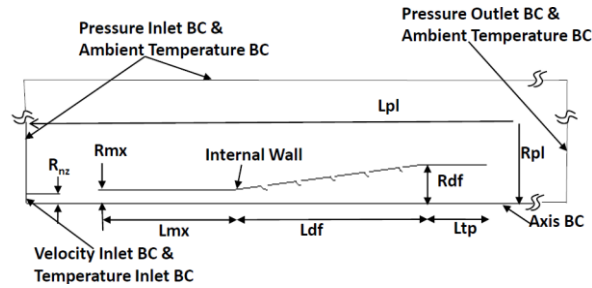


Fig. 3. Computational domain and boundary conditions.

of number of slots whereas marginal improvement in static pressure recovery was achieved for 10 slots. [Chen and Birk \(2009\)](#) worked on oblong shaped ejector diffuser and effect of swirl was studied. They compared the performance with conical straight ejector and found that for moderate swirl (30°) oblong shape performs better than conical shaped ejector diffuser.

While all these reported studies on ejector diffuser have indeed emphasized on the impact of shapes of ejector diffusers on the performance, to the best of authors knowledge no research has been carried out on the effects of specifically slot shapes and slot area on the performance of ejector diffuser. Slot shape and slot area are fundamental geometrical design parameters as they not only influence mass entrainment rate by changing flow characteristics around slots but also govern wall temperature resulting in superior infrared suppression device. Thus there is a need to perform systematic studies to improve an understanding of effects of slot shape and slot area. Such is the objective of this work. In the first part, investigations are performed on the effect of guided curve provided at each slot and its performance is compared with no guided curve at slots as shown in Fig. 2. The second part of study, covers the effects of slot area on the performance of guided-slot ejector diffuser and non-guided-slot ejector diffuser.

The paper is organized into six sections with first two sections being dedicated to abstract and introduction. Section 2. presents problem formulation, Section 3. presents plan of study highlighting performance indicators for ejector diffuser, Section 4. gives the results and discussion and Section 5. concludes the work with summary.

2. PROBLEM FORMULATION

This section describes the problem formulation in terms of (i) computational domain and boundary conditions, (ii) governing Eq.s and (iii) solver settings. Geometric outline for a guided-slot ejector diffuser and non-guided-slot ejector diffuser is shown in Fig. 2 to highlight the fundamental difference between them. It can be seen that slot shape in guided-slot case has guiding curve at all five slot openings. All other geometrical parameters are the same in two cases.

2.1 Computational Domain and Boundary Conditions

Two dimensional axi-symmetric computational

domain has been adopted for all simulations. The computational domain is shown in Fig. 3. Computational domain consists of (i) nozzle, (ii) standoff distance, (iii) mixing tube, (iv) slotted diffuser, (v) tail pipe and (vi) plenum. Description of various label used in Fig. 3 are listed in Table 1. Nozzle inlet (left side of domain) has been assigned velocity (normal to inlet) equal to 60m/s and a fixed temperature of 700°K . Axis boundary condition is imposed at the bottom boundary. The right, top and a portion of left side of the domain corresponds to plenum. Thus, atmospheric conditions are assigned on these boundaries. Walls of the nozzle, mixing tube and tail pipe are assigned no slip condition.

Table 1 Dimension of ejector diffuser Closure coefficients and Auxiliary Relations

Name	Value
D_{nz}	50mm
L_{nz}	$1D_{nz}$ (Singh et al. 2009)
L_{sd}	$2.25D_{nz}$ (Singh et al. 2017)
D_{mx}	$\sqrt{2.25}D_{nz}$ (Singh et al. 2017)
L_{mx}	$8D_{nz}$ (Singh et al. 2017)
L_{df}	$11D_{nz}$ (Sen 2008; Singh et al. 2009)
L_{tp}	$4D_{nz}$ (Sen 2008; Singh et al. 2009)
L_{pl}	$65D_{nz}$ (Chen, 2008)
D_{pl}	$21D_{nz}$ (Chen, 2008)
AR_{mx}	2.25 (Singh et al. 2017)
AR_{df}	8 (Singh et al. 2009)

A hybrid mesh comprising of quadrilateral and triangular cell elements has been used to generate mesh for both the cases. Mesh quality is monitored through aspect ratio where the value is maintained below 50. Further $y^+ < 1$ is achieved by placing first element at 0.02mm next to the wall. This will enable resolving the viscous sub layer as well.

2.2 Governing Equations

We employ steady-state Reynolds-averaged Navier-stokes (RANS) equations for our simulation. The RANS comprises of Reynolds averaged continuity (1), momentum (2) and energy (3) Eq.s:

$$\nabla \cdot (\rho \vec{v}) = 0; \quad (1)$$

$$\nabla \cdot (\rho \vec{v} \vec{v}) = -\nabla p + \nabla \cdot (\bar{\tau}); \quad (2)$$

$$\rho c_p (\vec{v} \cdot \nabla) T = k_{eff} \nabla^2 T; \quad (3)$$

where \vec{v} , p , ρ and T represent Reynolds-averaged velocity, pressure, density and temperature respectively. Symbol $\bar{\tau}$ represent total stress tensor where

$$\bar{\tau} = \mu^{eff} (\nabla \vec{v} + \nabla \vec{v}^T) \quad \text{and} \quad \mu^{eff} = (\mu + \mu_t) \quad (4)$$

Symbol μ^{eff} is sum of molecular viscosity (μ) and turbulent viscosity (μ_t) while k_{eff} is the effective conductivity and represent the sum of material thermal conductivity and turbulent thermal conductivity.

Previous studies by Singh *et al.* (2013), Sen (2008) and Chen (2008) on ejector diffuser has adopted different two-equation turbulence models: Standard k- ϵ (Launder and Spalding, 1974), Realizable k- ϵ (Shih *et al.* 1995) and SST k- ω (Menter, 1994). We select SST k- ω turbulence model due to its better performance in predicting velocity profiles against the experimental results of Sen (2008).

Equations (5) to (15) are additional set of equations in SST k- ω model for closure of RANS equations. Eq. (5) is the relationship between eddy (turbulent) viscosity and k (turbulent kinetic energy) and ω (specification dissipation rate) variables. Equations (6) and (7) are governing equations for k and ω , and Eqs. (8) to (15) give the closure coefficients and auxiliary relations for the SST k- ω turbulence models. The time derivative term is dropped in (6), (7) as the flow is statistically steady. Closure is achieved using the following equations:

$$\nu_t = \frac{a_1 k}{\max(a_1 \omega, S F_2)} \quad (5)$$

$$\nabla \cdot (\vec{v} k) = P_k - \beta^* k \omega + \nabla \cdot (v + \sigma_k v_T) \nabla k; \quad (6)$$

$$\begin{aligned} \nabla \cdot (\vec{v} \omega) = & \alpha S^2 - \beta \omega^2 + \nabla \cdot [(v + \sigma_k v_T) \nabla \omega] \\ & + 2(1 - F_1) \sigma_{\omega 2} \frac{1}{\omega} \nabla k \nabla \omega; \end{aligned} \quad (7)$$

Closure coefficients and Auxiliary Relations

$$F_2 = \tanh \left[\left[\max \left(\frac{2\sqrt{k}}{\beta^* \omega y}, \frac{500\nu}{y^2 \omega} \right) \right]^2 \right] \quad (8)$$

$$P_k = \min(\tau_{ij} \nabla \vec{v}, 10 \beta^* k \omega); \quad (9)$$

$$F_1 = \tanh \left\{ \left[\min \left[\left(\frac{\sqrt{k}}{\beta^* \omega y}, \frac{500\nu}{y^2 \omega} \right), \frac{4\sigma_{\omega 2} k}{CD_{k\omega} y^2} \right] \right]^4 \right\}; \quad (10)$$

$$CD_{k\omega} = \max \left(2\rho \sigma_{\omega 2} \frac{1}{\omega} \nabla k \nabla \omega, 10^{-10} \right); \quad (11)$$

$$\sigma_k = \frac{1}{F_1 / \sigma_{k1} + (1 - F_1) / \sigma_{k2}}; \quad (12)$$

$$\sigma_{\omega} = \frac{1}{F_1 / \sigma_{\omega 1} + (1 - F_1) / \sigma_{\omega 2}}; \quad (13)$$

$$\alpha = F_1 \alpha_1 + (1 - F_1) \alpha_2; \quad (14)$$

$$\alpha_1 = \frac{\beta_1}{\beta^*} - \frac{K^2}{\sigma_{\omega 1} \sqrt{\beta^*}} \quad \text{and} \quad \alpha_2 = \frac{\beta_2}{\beta^*} - \frac{K^2}{\sigma_{\omega 2} \sqrt{\beta^*}}; \quad (15)$$

$$\begin{aligned} \sigma_{k1} = 0.085, \sigma_{\omega 1} = 0.5, \beta_1 = 0.075, \sigma_{k2} = 1, \sigma_{\omega 2} = 0.856 \\ \beta_2 = 0.0828, \alpha_1 = 0.31, \beta^* = 0.09, K = 0.41 \end{aligned}$$

2.3 Solver Settings

Computational domain has been discretized using quadrilateral and triangular cells. Governing equations (Eqs. 1, 2, 3), equation for turbulent kinetic energy (k) and equation for specific dissipation rate (ω) are integrated over the discretized computational domain by finite volume technique (FVM). This gives a set of algebraic equations and with appropriate boundary conditions, they are solved using the Fluent Solver 15.0. For better accuracy, a 2nd order upwind scheme is employed to discretize the equations for momentum, k, ω and energy. However, in order to achieve convergence (convergence criteria of 10⁻⁶), a 1st order upwind scheme was initially used to obtain the solution. Then this converged solution is used as initial guess to obtain solution for 2nd order upwind scheme. SIMPLE algorithm is used for pressure velocity coupling to solve the pressure correction equation in an iterative method until convergence is achieved.

3. PLAN OF STUDY

The study aims to bring out the differences in the performance of conical ejector diffuser with guided and non-guided-slots. This is achieved by monitoring performance indicators as mentioned in this section.

3.1 Performance Indicators

Local mass entrainment ratio (κ) and Cumulative mass entrainment ratio (ϕ)

Local mass entrainment ratio (κ) is defined as ratio of mass entrained through a particular slot by nozzle exit mass flow rate as given by Eq. 16:

$$\kappa = \frac{m_{je}}{m_{in}}, \quad (16)$$

where m_{je} is entrained mass flow rate through slot openings and m_{in} is nozzle exit mass flow rate. Cumulative mass entrainment ratio (ϕ) is defined as ratio of cumulative mass entrained (secondary) through openings (stand-off and slots) to nozzle exit (primary) mass flow rate Kastner and Spooner (1950), Manganiello and Bogatsky (1976), Quinn (1959) as shown in Eq. 17:

$$\phi = \frac{\sum m_{je}}{m_{in}} \quad (17)$$

Normalized temperature variation (ψ)

The main source for infrared signature seeking missiles on a vehicle is the engine exhaust gases and the frame skin heated by the exhaust gases [Birk and Van-Dam \(1989\)](#), [Toulmay \(1988\)](#), [Mahulikar *et al.* \(2007\)](#). Normalized temperature variation (ψ) parameter will reveal extent of cooling at a given location of interest. It is defined as (Eq. 18):

$$\psi = \frac{T - T_0}{T_g - T_0}, \quad (18)$$

where T is the local temperature, T_0 is the ambient temperature and T_g is the temperature of exhaust gas at the nozzle exit. Plots of ψ at different axial length inside the ejector diffuser will also reveal mixing characteristics of primary and secondary flow streams. Likewise plots of ψ at ejector diffuser wall will reveal extent of cooling at the ejector diffuser walls. Plot of ψ at ejector diffuser exit will give overall temperature drop.

Coefficient of pressure recovery (C_p)

Coefficient of pressure recovery C_p represents diffuser capability to recover static pressure downstream compared to the inlet of the diffuser. It is defined as $C_p = \frac{p_{ex} - p_{in}}{q}$, where p_{ex} and p_{in}

are mass weighted averaged static pressure at the exit and inlet of a diffuser, while q represent inlet dynamic pressure. In the case of mass entraining ejector diffuser, C_p is modified to incorporate mass entrainment effect as suggested by [Nicoll and Ramaprian \(1970\)](#). The modified C_p is defined as:

$$C_p = \frac{(p_{ex} - p_{in})(m_{in} + \sum m_{je})}{\frac{1}{2}(\rho_{in}U_{in}^2 m_{in})} \quad (19)$$

3.2 Grid Independence and Validation Study

A grid independence study was conducted to obtain mesh independent results. Four grids having cell counts between 0.6 million to 1.1 million (Mesh 1 = 600000, Mesh 2 = 770000, Mesh 3 = 920000 and Mesh 4 = 1100000) were tested at fixed Reynolds number $Re_{nz} = 1.3 \times 10^5$ using SST k- ω turbulence model. Axial velocity profiles downstream of 3rd slot is plotted using results from the four grids are shown in Fig. 4. Velocity profiles for Mesh 3 and Mesh 4 match exactly with each other, and hence cell count of Mesh 3 is selected for the current study.

To validate our numerical methodology we compare the numerical results obtained for a conical step-slot ejector diffuser against the available experimental

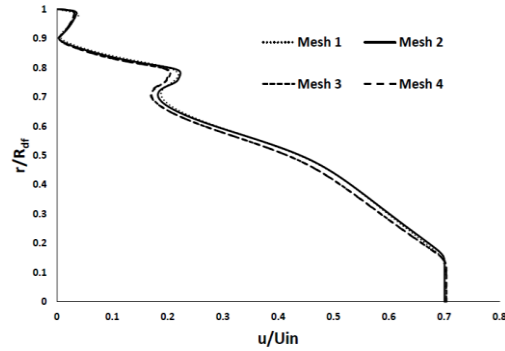


Fig. 4. Axial velocity profile comparison downstream of 3rd slot.

results of [Sen \(2008\)](#). Figure 5 compares the axial velocity profiles upstream of the first slot. Three turbulence models (Standard k- ϵ , Realizable k- ϵ and SST k- ω) were selected based on the literature review and compared with the experimental results of ([Sen, 2008](#)). In the shear region close to the wall, all turbulence models shows similar extent of deviation from the experimental data. However, at the core Realizable k- ϵ shows maximum deviation of 4% while SST k- ω shows better matching (< 1%). The performance of Standard k- ϵ is observed to be intermediate.

We observe that the difference among the three turbulence models are not very significant. However, SST k- ω shows least deviations. Hence, SST k- ω is the choice to carry out the present simulation study.

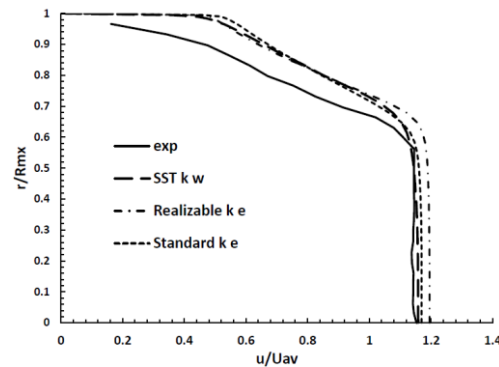


Fig. 5. Comparison between the predicted results with the experimental results of [Sen \(2008\)](#).

4. RESULTS AND DISCUSSION

Numerical study has been conducted on guided-slot and non-guided-slot ejector diffuser and results are presented in two parts. Part I (Section 4.1) discuss results for effect of guided-slot and Part II (Section 4.2) gives the effect of slot area. In both parts, performance indicators are evaluated as per the plan described in Section 3.

4.1 Effect of Guided Slot

To bring out the impact of guided-slot over conventional ejector diffuser, guided-slot constant

area ejector diffuser (GCAED) and non-guided-slot constant area ejector diffuser (NGCAED) have been compared in terms of performance parameters, flow and heat transfer characteristics. The choice of constant slot area condition will help in highlighting the effect of guided-slot only and nullify any change in slot area effects on the performance. Geometrical detailing for both the cases are same except the presence of guided-slot in GCAED as shown in Fig. 2. The dynamical parameters such as nozzle inlet Reynolds number, inlet turbulence intensity, inlet turbulence length scale, nozzle inlet fluid temperature are kept the same. Similarly the boundary conditions, plenum size and ambient conditions are identical for the two cases.

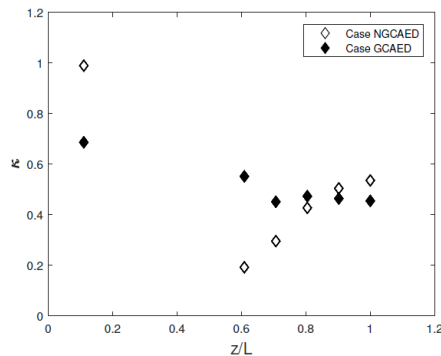


Fig. 6. κ for GCAED and NGCAED.

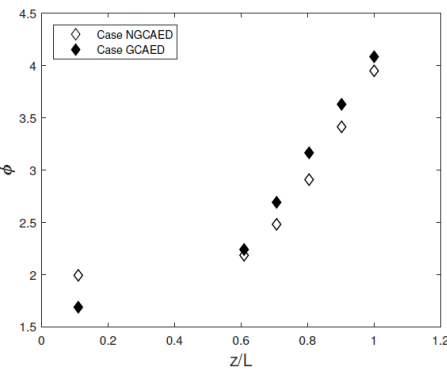


Fig. 7. ϕ for GCAED and NGCAED.

4.11 Local Mass Entrainment Ratio and Cumulative Mass Entrainment Ratio

Effect of guided-slot on local mass entrainment ratio (κ) and cumulative mass entrainment ratio (ϕ) has been numerically studied and results for both are presented in this section. Figure 6 compares the local mass entrainment ratio (κ), whereas Fig. 7 compares the cumulative mass entrainment ratio (ϕ) for the two cases. In Fig. 6 and 7, x-axis represents non-dimensional axial length where z is the local axial length and L is the overall ejector diffuser length. Figure 6 shows that the entrainment through the standoff distance is higher for the NG-CAED compared to the GCAED but the entrainment for NGCAED falls drastically at the 1st slot in the diffuser part. Thereafter it increases linearly up to the 3rd slot and further downstream the rate of entrainment drops significantly. For GCAED, the

entrainment through the 1st slot falls marginally and there after remains nearly constant at the other slots. At $z/L=0.11$, which represents the location after standoff distance, entrainment through the standoff distance is higher for the NGCAED ($\kappa = 0.99$) compared to the GCAED ($\kappa = 0.68$) as seen from Fig. 6. Further downstream, the entrainment for NGCAED falls drastically, from $\kappa = 0.99$, to $\kappa = 0.19$ at the 1st slot ($z/L=0.6$) in the diffuser. Thereafter the entrainment at the 2nd slot increases to $\kappa = 0.29$ and is 54% higher compared to the 1st slot. At 3rd slot $\kappa = 0.43$ shows 44% increase over 2nd slot. At the 4th slot $\kappa = 0.5$ shows an increase of only 18% and at the last slot $\kappa = 0.53$, an increase of only 6% from the previous slot. It shows that after the 1st slot there is a large entrainment from 2nd and 3rd slot but the same is not seen at 4th and 5th slot. Similar observations for GCAED reveals that entrainment through 1st slot drops only by 24% to $\kappa = 0.55$ compared to entrainment through SD. At 2nd slot, a drop of 4% in κ is observed and there after κ remains more or less constant at the other slots. To understand this phenomena we examine the mechanism of entrainment. The entrainment through any opening takes place because of pressure differential across the opening (Ricou and Spalding, 1961) and transfer of momentum between two streams moving at different speeds at the shear layer. The mass entrainment through standoff distance is more for NGCAED because the flow velocity in the mixing tube is accelerating at a higher rate compared to the GCAED as shown in Fig. 8. The reason for such a behaviour is the upstream effects of the guiding curve for GCAED which affects the local upstream pressure distribution due to the blockage effect. Fig. 9 depicts the pressure contour plot for the two cases in the region of standoff distance. It can be seen that static pressure values for NGCAED fall to -700 Pa compared to -300 Pa for GCAED. The higher static pressure difference and dominant shear layer action for the NGCAED leads to higher mass entrainment through SD. The entrainment phenomena in the diffuser is dominated by either single or both mechanisms. For the NGCAED, the entrainment through the 1st slot is small because this entrainment is dominated by the shear layers entrainment whereas in the downstream slots, the entrainment through slots is because of pressure differential which is the highest for the last slot and hence higher entrainment (Fig. 10). For GCAED entrainment is dominated by shear layer action because of the higher acceleration of flow velocity by the guiding curve at each slot which results in nearly constant entrainment through each slot. Fig. 11 is a plot where axial velocity at the downstream of 1st slot reveals a typical difference in axial velocity profile for guided-slot and non-guided-slot cases where a shear layer action being present only for the GCAED. At the end of 5th slot, Fig. 7 shows the cumulative mass entrainment ratio for both the cases, and it is seen that cumulative mass entrainment increases continuously,

the rate of increase being slightly higher for GCAED. The final value of ϕ after the 5th slot for GCAED is $\phi = 4.1$ and for NGCAED it is $\phi = 3.9$. This represents an increase of 3.5% for guided-slot constant area ejector diffuser over the non-guided-slot constant area ejector diffuser. Hence guided-slot design offers better mass entrainment characteristics.

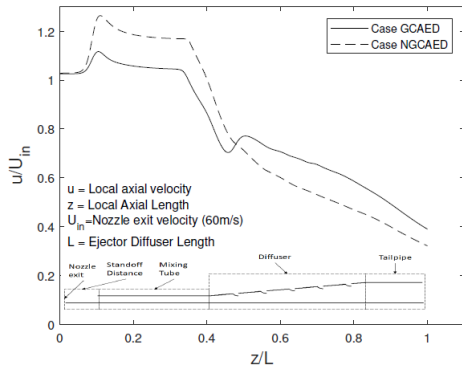


Fig. 8. Axial velocity at the axis of ejector diffuser.

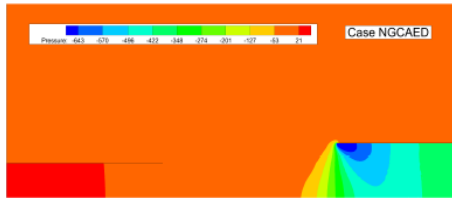
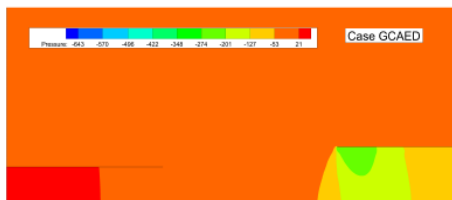


Fig. 9. Pressure contours near standoff zone.

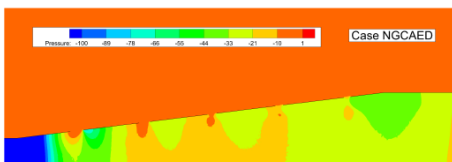
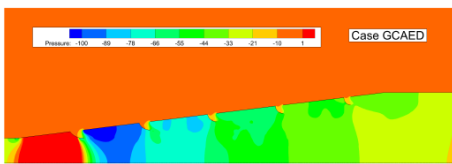


Fig. 10. Pressure contours inside diffuser part.

4.12 Normalized Temperature Variation

Study of temperature distribution in the two cases, GCAED and NGCAED, is presented in this section. For both the cases, exhaust jet temperature at nozzle exit is 700°K and ambient air temperature is 300°K . Reynolds number for the study is $Re = 1.3 \times 10^5$. To understand the effect of guided-slot on the

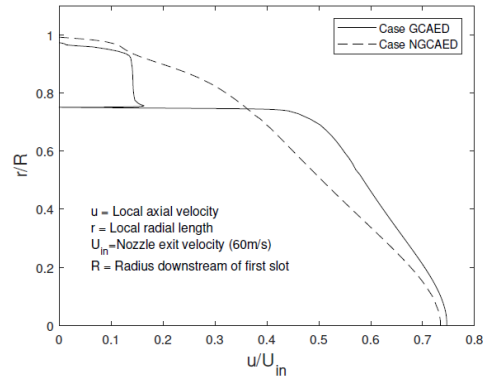


Fig. 11. Axial velocity downstream of 1st slot.

temperature distribution and thermal mixing in an ejector diffuser, normalized temperature variation (ψ) parameter is investigated in three stages (i) along the axis of ejector diffuser, (ii) along the radial direction after every slot and (iii) along the diffuser wall for the two cases.

Figure 12 is a plot between ψ and non-dimensional ejector diffuser axial length on the symmetric axis. For both the cases, core temperature (700°K) is maintained for large part of the mixing tube ($0.096 < z/L < 0.403$) which indicates that entrainment through standoff distance does not affect temperature at the core within the mixing tube. For GCAED, core temperature starts to drop slightly before NGCAED. These locations also represent disappearance of the potential core for the two cases. For diffuser region $0.403 < z/L < 0.867$, both the cases shows temperature drop along the diffuser axis. But GCAED retains little higher core temperature due to gain in momentum at guiding curves at each slot. Although, the temperature drop is at a steady rate for the two cases, at the end of ejector diffuser ψ for NGCAED is 0.343 and ψ for GCAED is 0.363 which shows that NGCAED has marginally ($< 3\%$) lower core temperature compared to GCAED.

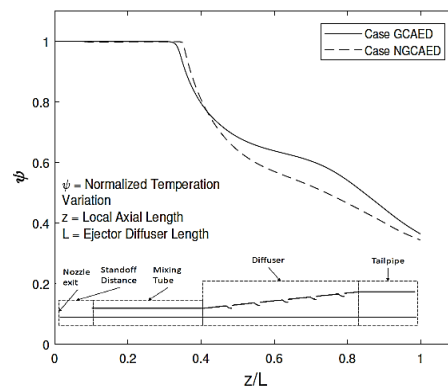


Fig. 12. ψ along the axis of ejector diffuser.

The effect of guided-slot (GCAED) on temperature distribution inside the diffuser and tail pipe section can be understood by investigating temperature contours shown in Fig. 13. Temperature range is set to $500 < T < 300$ for the better viewing of local temperature variations. At the core of diffuser, hot

fluid zones can be seen for both the cases. Towards end of diffuser section and initial part of the tailpipe section the hot zones start to disappear. The disappearance of hot zone is little early for NGCAED compared to GCAED. Figure 13 also reveals that as hot fluid exit the mixing tube and enter into the diffuser it tries to expand along the wall. Expansion of the hot fluid jet stream to the diffuser wall is encountered by entraining stream of cold flow from the 1st slot. This leads to diversion of hot fluid away from the wall as seen in Fig. 13. Diversion of hot fluid away from diffuser wall is present in both cases. But for GCAED, diversion is more noticeable at 1st slot as a physical wall in the form of guided-slot diverts the hot fluid. The diversion of hot fluid in both cases impacts local mixing of hot fluid with cold entrained fluid. Local temperature variation along the radial direction in the diffuser after every slot allows a better understanding of the temperature variation. Same is shown in Fig. 14. Figure 14a high-lights radial lines along the diffuser length where local temperature values are extracted. In Fig. 14b (location BB (Fig. 14a) after 1st slot) a large annulus region $0 < r/R < 0.6$ at the core is dominated with hot fluid where ψ varies between 0.6 and 0.7. This is true for both the cases. For $r/R > 0.6$, the value of ψ drops significantly upto $r/R = 0.7$ for GCAED depicting large temperature drop, whereas no steep temperature drop is seen for NGCAED. For range $0.7 < r/R < 1$ GCAED has lower value of ψ ranging between 0 to 0.1 which shows that temperature near the wall is close to ambient conditions. For NGCAED ψ varies between 0.2 to 0.3 which means higher wall temperature compared to GCAED. Overall at Location BB, large variation of ψ is observed for GCAED whereas for NGCAED, there is relatively more uniform thermal mixing. At Location CC (Fig. 14c), similar ψ profiles are obtained as that at Location BB. Although for GCAED high $\psi > 0.6$ values are limited to range $0 < r/R < 0.4$ and then steep ψ gradients are present over range $0.4 < r/R < 0.75$. Thus, mixing at Location CC is enhanced compared to Location BB. The trends of enhanced mixing are also observed for subsequent locations as can be seen from Fig. 14d-14f. At Location FF, ψ profile for both cases overlaps with each other having marginal variations. Thus guided-slot case offers lower temperature zones

close to the walls.

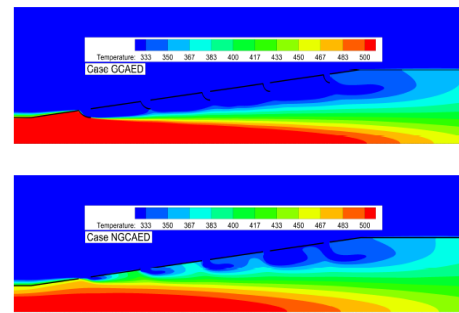


Fig. 13. Temperature contour inside the diffuser part.

Heated diffuser wall can act as a heat source and heat transfer to the surrounding metal body can become potential IR source for heat seeking missile [Toulmay \(1988\)](#), [Mahulikar *et al.* \(2007\)](#). Fig. 15 is a plot between non dimensional wall temperature (T_w) normalized with entrained fluid temperature (T_0) along the ejector diffuser wall. It is seen that for GCAED, wall temperature tends to increase along the mixing tube upto $z_w/L_w = 0.4$ whereas for NGCAED the wall temperature also increases in the mixing tube but has lower values. This behaviour is associated to higher mass entrainment through SD (Fig. 6). Along diffuser wall, GCAED has lower wall temperatures and it is of the order of entrained fluid temperature $T_0 = 300^\circ K$. For NGCAED, wall temperature ratio varies in the range $1.1 < T_w/T_0 < 1.3$, and it indicates higher diffuser wall temperature. The same effect can be seen in Fig. 13 where close to diffuser wall, cold pockets are formed for GCAED unlike in NGCAED. Formation of cold pockets near the diffuser walls in GCAED is explained by comparing streamline plot for the two cases in Fig. 16. While streamline indicates flow direction, the colour of the streamlines indicates temperature magnitude. Due to the guided-slot, entrained fluid gets directed towards the diffuser wall. Further the guided entrained fluid encounters the next guided-slot. This leads to the formation of recirculation pockets below diffuser wall in the GCAED. This phenomenon is absent for NGCAED. Thus cold zones are formed below diffuser wall only for the GCAED and not for NGCAED.

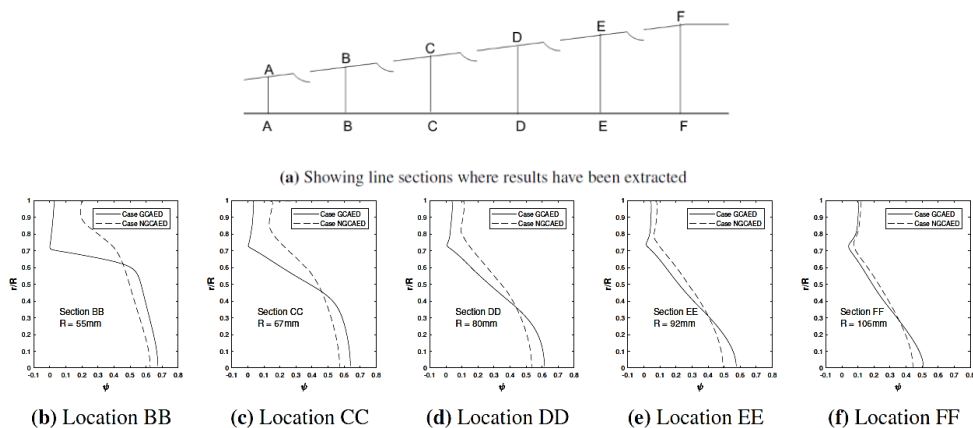


Fig. 14. Comparison of ψ at multiple locations inside diffuser.

4.13 Static Pressure Recovery

The role of a diffuser is to recover static pressure. Static pressure recovery is estimated by calculating the static pressure coefficient C_p . Equation 19 gives the definition of C_p for ejector diffuser which primarily is the difference of static pressures at a given axial location in the diffuser and static pressure at the inlet of the mixing tube divided by dynamic pressure at the inlet of the mixing tube. Equation 19 also takes into account the mass entrainment effect.

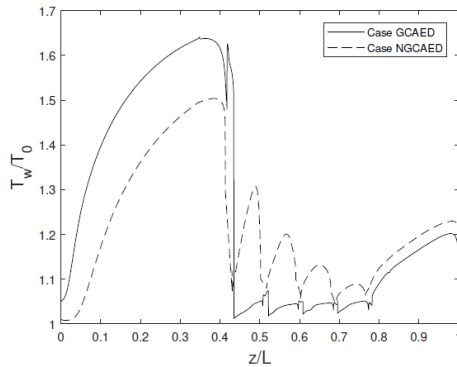


Fig. 15. Ejector diffuser wall temperature distribution.

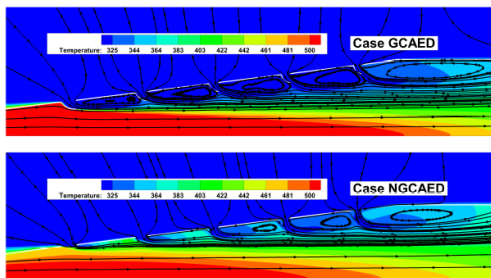


Fig. 16. Streamlines for GCAED and NGCAED.

Figure 17 shows the variation of C_p along the length of the ejector diffuser for NGCAED and GCAED. The static pressure at any axial location is the mass-weighted averaged value. It is observed from Fig. 17 that NGCAED has overall higher $C_p = 0.79$ than GCAED where $C_p = 0.43$ at the exit. However, a closer inspection reveals that C_p is higher for GCAED ($C_p = 0.175$) than NGCAED ($C_p = 0.07$) in the mixing tube ($0 < z/L < 0.4$). This could be due to the higher entrained mass through the standoff distance for NGCAED. At the 1st slot in the diffuser ($0.46 < z/L < 0.57$), GCAED shows a significant fall in C_p value from 0.31 to 0.11. Any such dip in C_p values for the NGCAED is not seen. Drop in C_p can be associated with the presence of guided-slot which acts as a physical blockage to incoming stream and effectively there is no increase in area vis a vis NGCAED. This leads to increase in velocity of the fluid thereby reducing the static pressure. Figure 18 compares the pressure contours for the two cases. It is seen that for GCAED large

pressure variations ranging from -85Pa to 195Pa are present over a small region whereas no such pressure variation is seen for the NGCAED. From $z/L=0.57$ (Fig. 17) onwards static pressure recovery in the GCAED happens in a very similar way as in the NGCAED and the curves are nearly parallel. This implies that effective diffusion for GCAED starts after the 1st slot. Close observation of the diffuser geometry and the pressure variation seen in the two geometries suggest that an additional slot in GCAED will result in similar pressure recovery. This can be evaluated by comparing the pressure recovery upto 5th slot for GCAED and 4th slot for NGCAED. The two values are 0.43 and 0.65 respectively. This also suggests that the mass entrainment is higher in GCAED compared to NGCAED leading to lower pressure recovery which is opposite of the trend of pressure recovery in the mixing tube. The difference observed in pressure recovery is too large to be only due to mass entrainment. The other reason could be due to loss of energy at each slot as a result of expansion before the guiding curve and then contraction as it passes over the guiding curve.

As highlighted in the literature review, there is no open literature where study on slot-guidance has been reported. Thus, a direct comparison of our results is not possible. However, some work has been reported on step-slots which is compared with our work.

Two non-dimensional performance parameters ϕ and C_p of our slot-guided ejector diffuser can be compared with the corresponding values obtained by Singh *et al.* (2016) in the case of rectangular step-slot ejector diffuser and those obtained by Chen and Birk (2009) in the case of oblong step-slot ejector diffuser. We find $\phi = 4.1$ for our simulation and is higher than ϕ obtained by Singh *et al.* (2016) $\phi = 3.2$ and Chen and Birk (2009) $\phi = 2.25$. In case of pressure recovery, $C_p = 0.43$ obtained in guided-slot ejector diffuser is comparable to $C_p = 0.46$ for the rectangular step-slot ejector diffuser but higher than the $C_p = 0.3$ obtained in oblong step-slot ejector diffuser.

4.2 Effect of Slot Area

The effect of slot area (increasing and decreasing) on the performance parameters (Section 3.) for guided-slot ejector diffuser and non-guided-slot ejector diffuser (Fig. 2) is presented. Ejector diffuser has five slot openings, and each slot opening has varying area. Slot area is defined as the projected area of the opening on the plan perpendicular to the diffuser axis. Effect of slot area is investigated by varying it for five slots in a systematic manner by (i) increasing the slot area (IA) and (ii) decreasing the slot area (DA) as given in Table 3. The results has been compared with constant area slots. A guided-slot increasing slot area ejector diffuser is referred as GIAED. Likewise, non-guided- slot increasing slot area ejector diffuser is referred as NGIAED. Similarly for decreasing area (DA), the

Table 2 gives a comparative analysis between the guided-slot and no-guided-slot ejector diffuser.

Performance parameter	Advantages	Disadvantages
Local mass entrainment	Higher mass entrainment through the first slot (see Figure 6)	Lower mass entrainment through the stand-off gap (see Figure 6)
Cumulative mass entrainment	3.5% more mass entrainment (see Figure 7)	—
Wall temperature	Closer to ambient conditions (see Figure 15)	—
Centerline temperature at the ejector diffuser exit	—	Marginally lower temperature (by 3%) (Figure 12)
Thermal exit profile	Area-weighted average ψ drop > 4%	—
Static pressure recovery	—	Lower pressure recovery by 33% (see Figure 17)

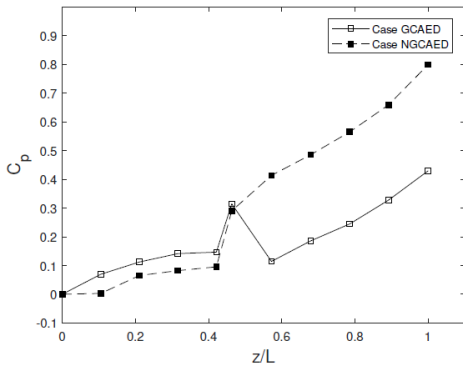


Fig. 17. C_p at different axial location along the ejector diffuser for NGCAED and GCAED.

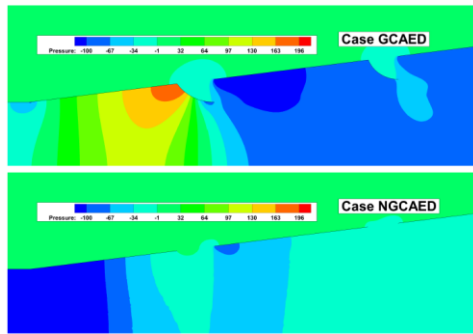


Fig. 18. Static pressure distribution around 1st slot region for GCAED and NGCAED.

cases are GDAED and NGDAED. To understand the effect of slot area on the performance of guided-slots and non-guided-slots ejector diffuser, guided-slot cases are compared to non-guided-slot cases. Further all guided-slot cases are referred as Set-I and non-guided-slot cases as Set-II. Reynolds number, boundary conditions, and solver setting is consistent for all the cases. The study is divided into three sections where performance parameters are compared.

Table 3 Slot area values. IA(Increasing area), CA (Constant area), DA(Decreasing area)

Slot	1 st	2 nd	3 rd	4 th	5 th
IA	A_0	$1.26A_0$	$1.51A_0$	$1.77A_0$	$2.02A_0$
CA	A_0	A_0	A_0	A_0	A_0
DA	A_0	$0.87A_0$	$0.75A_0$	$0.62A_0$	$0.49A_0$

4.21 Local Mass Entrained Ratio and Cumulative Mass Entrained Ratio

Effect of slot area on local mass entrainment ratio (κ) and cumulative mass entrainment ratio (ϕ) have been

discussed in this section. Figure 19 highlights the effect of slot area on κ for guided-slot cases (Set-I) and Fig. 20 highlights the effect of slot area on κ for non-guided-slot cases (Set-II). At $z/L=0.11$, κ for Set-I cases (Fig. 19) overlaps with each other showing same amount of mass entrainment happens for all three cases from the standoff distance. This means that change in slot area downstream in the diffuser has no upstream effect on mass entrainment. Similar effect is seen for Set-II cases (Fig. 20). However at the 1st slot, $z/L=0.61$, effect of slot area on the mass entrainment can be seen for Set-I wherein mass entrainment for constant slot area is $\kappa = 0.55$. However, for other two cases it is nearly same ($\kappa=0.48$). Similarly for Set-II, variation in mass entrainment is observed between $0.16 < \kappa < 0.19$ with value being highest for constant slot area and minimum for increasing and decreasing slot area. Even though the slot area is same (A_0) for all the cases there exist differences in mass entrainment through 1st slot. This observation indicates that there is an effect of the downstream change in slot area on the mass entrainment through 1st slot. Another observation reveals that κ for both the sets (Set-I and Set-II) is higher for constant slot area (GCAED and NGCAED).

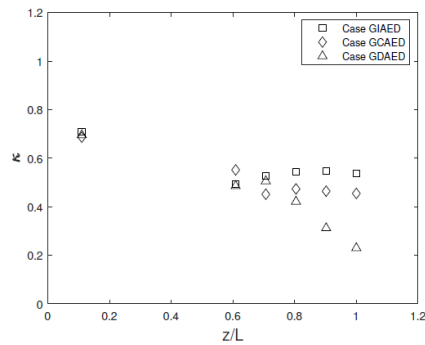


Fig. 19. Comparison of κ for Set-I.

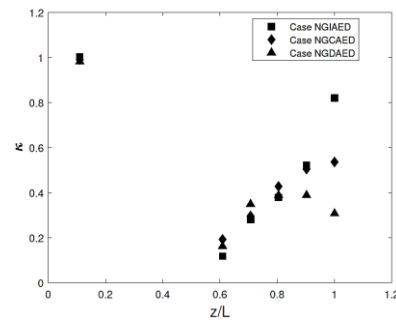


Fig. 20. Comparison of κ for Set-II.

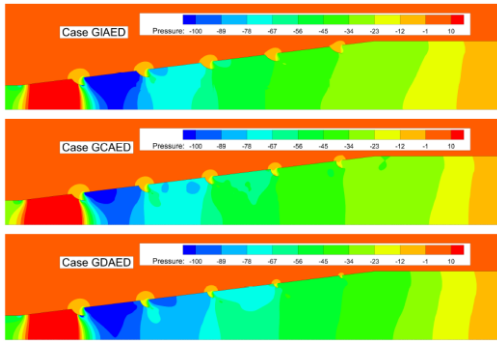


Fig. 21. Pressure contour for GIAED, GCAED and GDAED.

Close observation of Fig. 19 depicts a drop in mass entrainment by 22% for GCAED whereas GIAED and GDAED show an increase in mass entrainment by 6% and 4% respectively at the 2nd slot. After 2nd slot, the mass entrainment keeps increasing upto 4th slot and then drops for GIAED. The mass entrainment in GCAED increases marginally upto 3rd slot and then remains constant whereas it drops significantly for GDAED. This behaviour can be understood by looking at the plausible mechanism of mass entrainment which is governed by pressure differential near the slot and shear layer action between the primary and entrained fluid. To investigate pressure differential, a plot of pressure contours for Set-I cases are shown in Fig. 21. It can be seen that higher pressure differential ($\Delta p \approx 100$ Pa) are present for GIAED and GDAED at 2nd slot while for GCAED lower pressure differential ($\Delta p \approx 50$ Pa) exists. Shearing action due to primary fluid for GIAED and GDAED is stronger compared to GCAED. Further downstream, the pressure differential is nearly constant for GIAED and GCAED, whereas it reduces for GDAED. The pressure differential implies that the mass entrainment through GIAED is purely an effect of increased area. The reduction in mass entrainment is effect of both decreasing area and pressure for GDAED. The behaviour of local mass entrainment through 2nd slot for Set-II cases (Fig. 20) is completely different from Set-I cases. The mass entrainment for all the cases in Set-II increases in 2nd slot compared to 1st slot with NGDAED showing higher mass entrainment than other cases. This can be explained observing pressure contour plots (Fig. 22). We observe that the highest pressure differential is for NGDAED at 2nd slot. Mass entrainment increases for all the three cases at the 3rd slot, but the rate of increase is less compared to 2nd slot.

At 4th slot, NGDAED shows no increase in mass entrainment while other two cases show a very similar increase in κ . At 5th slot, NGDAED shows drop in mass entrainment, NGCAED records no increase in mass entrainment and NGIAED shows significant increase in mass entrainment. So downstream of the diffuser part the decreasing area slot shows a similar trend to Set-I cases, wherein higher slot area has higher mass entrainment. Figure 23 and Fig. 24 shows the cumulative mass entrainment ratio for Set-I and Set-II, respectively at

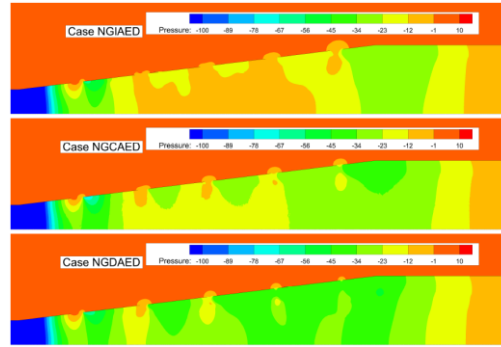


Fig. 22. Pressure contour for NGIAED, NGCAED and NGDAED.

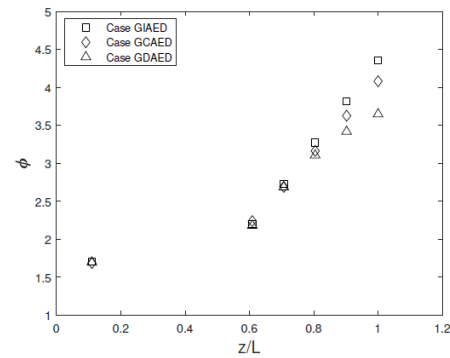


Fig. 23. Comparison of ϕ for Set-I.

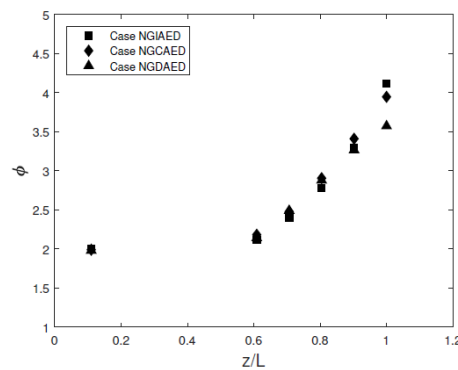


Fig. 24. Comparison of ϕ for Set-II.

the end of 5th slot. The cumulative mass entrainment ratio (ϕ) can be seen increasing for both Set-I and Set-II. At the downstream of the diffuser, rate of increase seems to depend upon slot area. Increasing slot area cases of Set-I and Set-II shows maximum ϕ . Value of ϕ for GIAED is 4.35 which is 20% more than GDAED. Similarly for NGIAED is ϕ is 4.12 which is 15% more than NGDAED. Hence increasing slot area shows higher mass entrainment.

4.22 Effect of Slot Area on Temperature Variation

Study of temperature distribution for six cases has been conducted and results are presented in this section. Nozzle exit temperature (T_g) is maintained

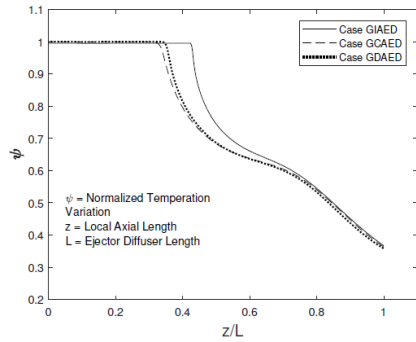


Fig. 25. ψ at ejector diffuser axis for Set-I.

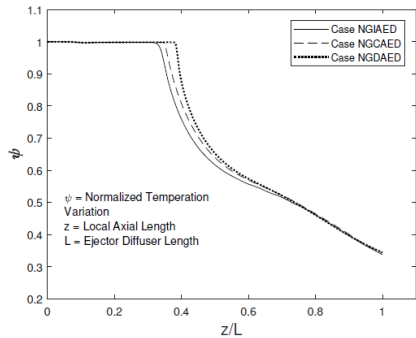


Fig. 26. ψ at ejector diffuser axis for Set-II.

at 700°K while atmospheric temperature (T_0) is maintained at 300°K for all six cases. Reynolds number of $Re = 1.3 \times 10^5$ is fixed for all cases. Results are presented in terms of non-dimensional parameter ψ , defined in Section 3. To understand the effect of slot area on ψ in the core region of ejector diffuser, plot for Set I and Set II cases are shown in Fig. 25 and Fig. 26, respectively. Within mixing tube ($0.08 < z/L < 0.4$) nozzle exit temperature $\psi=1$ is conserved for a large section of mixing tube. This is seen for all the cases. It implies that mass entrainment through standoff distance does not affect centreline (axis) temperature of the mixing tube. The

location of the fall in ψ starts to appear close to the exit of mixing tube. However, this location is different for every case of Set I (Fig. 25) and also for cases of Set II (Fig. 26). It reflects the effect of slot area on ψ at the axis of the ejector diffuser. For Set-I, GIAED retains $\psi=1$ for the longest length ($z/L=0.43$) while for Set-II, NGDAED retains $\psi=1$ till $z/L=0.39$. Downstream of ejector diffuser ($z/L > 0.7$) no difference of ψ is observed within Set-I and same is true for Set-II. This shows that upstream effects of difference in ψ between the two sets does not influence the ejector diffuser performance on the axis. Thus the change in slot area has no effect on centreline temperature distribution on the axis towards the exit of ejector diffuser.

For understanding the effect of slot area on local thermal mixing, ψ has been plotted within diffuser at multiple radial locations. Plot locations are shown in Fig. 14a where Location BB represent radial length after 1st slot and Location FF represent radial length at diffuser exit. Fig. 27a-27e presents comparison of ψ for Set-I while Fig. 27f-27j presents comparison of ψ for Set-II. It can be seen that for both the sets, Location BB, CC and DD ψ profiles for IA, CA and DA do not have a noticeable difference. However, at Location EE and FF, visible changes in ψ profiles start to appear close to the wall. Also, the Location FF is close to the exit of an ejector diffuser, hence it reflects performance regarding overall temperature drop. For Set-I, Fig. 27e, annular region at the core $0 < r/R < 0.4$ for the three cases shows similar ψ depicting similar temperature values. For range $0.4 < r/R < 1.0$ GDAED has higher ψ than others. A mass-weighted averaged value of static temperature at Location FF gives GDAED= 400°K , GCAED= 395°K , and GIAED= 388°K . It reflects the impact of slot area and IA showing better temperature drop as well as a better radial profile at diffuser exit. Similarly for Set-II (Fig. 27j) mass-weighted average value of static temperature at Location FF gives NGDAED= 405°K .

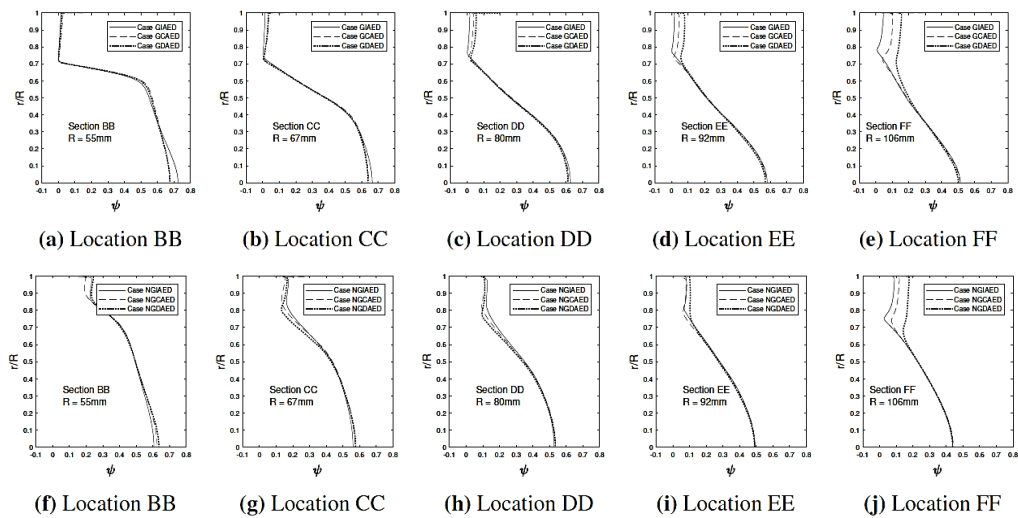


Fig. 27. Comparison of ψ at multiple locations inside diffuser.

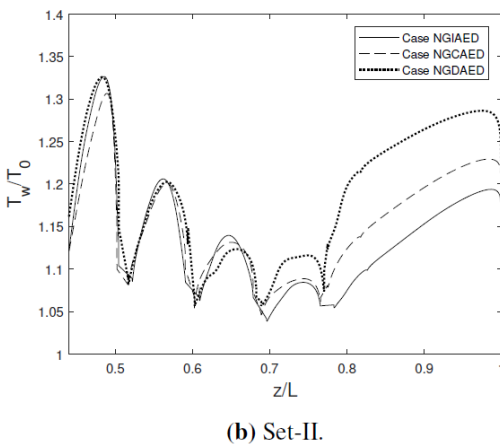
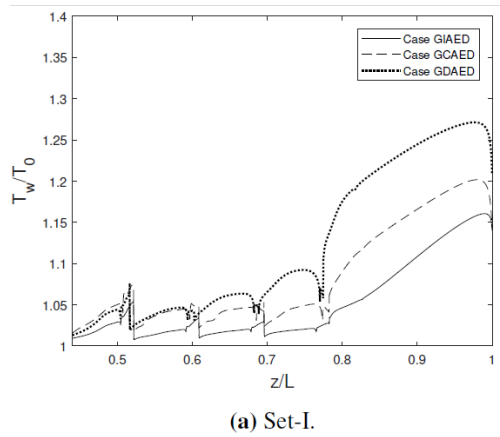


Fig. 28. Normalized wall temperature.

$^{\circ}\text{K}$, $\text{NGCAED}=397^{\circ}\text{K}$, and $\text{NGIAED}=391^{\circ}\text{K}$. Hence IA in both sets has overall higher drop in temperature.

Further, the effect of slot area on wall temperature is analysed, and results are presented in Fig. 28a for Set-I and in Fig. 28b for Set-II. From both the plots, normalized wall temperature downstream of 1st slot ($z/L > 0.44$) depicts the effect of slot area downstream of ejector diffuser. For Set-I, effect of slot area can be seen because the normalized wall temperature profiles do not overlap with each other. For Set-II, temperature profile overlap over the range $0.44 < z/L < 0.7$ (upto 3rd slot). This highlights that in the range $0.44 < z/L < 0.7$, effect of slot area for guided-slot cases is more than non-guided-slot cases. Further, for Set-I, GIAED shows lower T_w/T_0 value than other cases, and this trend is observed throughout the wall length. The wall temperature gap between the three cases keeps on widening towards the exit of the diffuser.

For Set-II, difference in T_w/T_0 starts to appear after $z/L > 0.7$. NGIAED shows lower temperature values with NGDAED having highest wall temperature values. The results shows that, increasing slot area case shows better wall cooling capabilities for both the sets.

4.2.3 Effect of Slot Area on Static Pressure Recovery

Effect of slot area on coefficient of pressure recovery C_p is studied in this section. Figure 29a represents Set-I and Fig. 29b represents Set-II. For both sets, C_p for IA, CA and DA cases in the mixing tube $0 < z/L < 0.42$ have similar values. Thus, the slot area has negligible upstream effect on C_p for all cases (Set I and Set II).

In diffuser section ($0.42 < z/L < 1$), the effect of slot area on C_p is noticeable for both sets. For Set-I (Fig. 29a), GIAED has maximum $C_p = 0.48$ at the end of ejector diffuser while GDAED has lowest $C_p = 0.33$. Thus for the guided-slot cases, IA offers maximum pressure recovery. Equation 19 shows that C_p depends on mass-weighted averaged static pressure as well as mass entrainment rate at any particular location. It has been shown in Section 4.2.1 that IA cases offer superior mass entrainment rate than other cases and it translates into higher C_p . However for non-guided-slot cases (Set II), NGCAED returns highest C_p while NGDAED has lowest C_p .

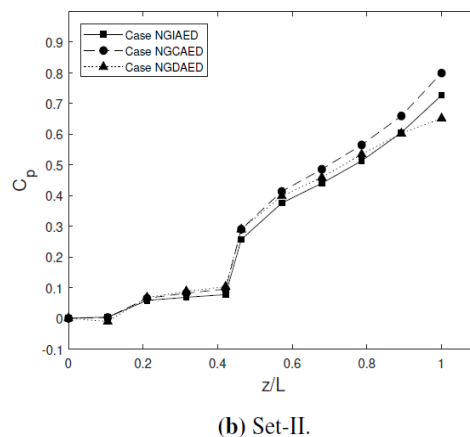
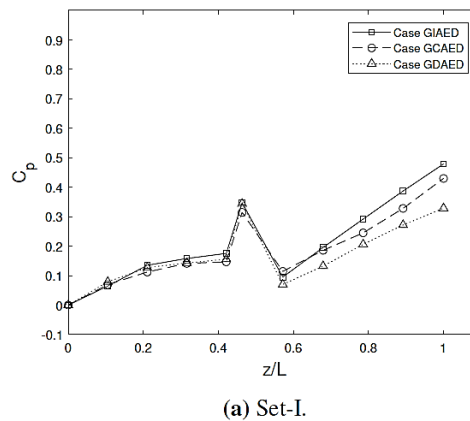


Fig. 29. Comparison of C_p .

5. CONCLUSION

Ejector diffuser is a device employed as an infrared suppression system in combat vehicles such as helicopters, aircrafts, ships, etc. It suppresses infrared signatures by bringing down the temperature of exhaust gases through mass entrainment. Mass entrainment take place through strategic openings (standoff distance and slot openings) on the surface of ejector diffuser. Based on literature survey it has been found that only step slot openings have been studied. In the current study, investigation of a new slot shape in the form of guided-slots is undertaken and its performance is compared with non-guided-slot ejector diffuser. Secondly, the effect of slot area for guided and non-guided slot ejector diffuser is investigated. Major conclusions of the work are:

1. Keeping all geometric and dynamical parameters consistent, guided-slot case (GCAED) achieves higher cumulative mass entrainment (> 3.5%) over non-guided-slot case (NGCAED).
2. Centerline axial temperature profile for GCAED and NGCAED tends to overlap towards the exit of ejector diffuser.
3. Radial temperature profiles for GCAED shows annulus region close to the wall with significant lower temperature values. Any such low-temperature region is not observed for NGCAED.
4. Lower wall temperature is present throughout the diffuser wall (nearly 300 °K) for the guided-slot ejector diffuser whereas the same is not true for non-guided-slot ejector diffuser.
5. Static pressure recovery is smaller (33.8%) for guided-slot ejector diffuser in comparison to non-guided-slot ejector diffuser.
6. Study of slot area reveals that increasing slot area achieves higher mass entrainment upto 20% over constant and decreasing slot area ejector diffuser. Further, the lower wall temperature is observed for increasing area ejector diffuser.
7. No advantage of increasing or decreasing slot area is seen on the centerline axial temperature as all cases tend to overlap with each other.
8. For guided-slot ejector diffuser, increasing slot area has better static pressure recovery upto 45% more over the other two cases. For non-guided-slot ejector diffuser, constant slot area case has a marginally better pressure recovery than the other two cases.

The study is expected to offer an alternate design for an ejector diffuser having in line slot opening with guidance and no guidance. The guided-slot ejector diffuser leads to higher mass entrainment as well as better cooling capabilities at the expense of slightly lower pressure recovery. So it can be concluded that even though there is a drop in pressure recovery for guided-slot ejector diffuser, there is an overall gain in terms of infrared suppression capabilities.

Pressure recovery is superior for inline slot ejector diffuser than the guided-slot ejector diffuser.

REFERENCES

- Barik, A. K., S. K. Dash, and A. Guha (2015). Experimental and numerical investigation of air entrainment into an infrared suppression device. *Applied Thermal Engineering* 75, 33–44.
- Birk, A. and D. VanDam (1989). Marine gas turbine infra-red signature suppression: Aerothermal design considerations. *ASME 1989 International Gas Turbine and Aeroengine Congress and Exposition*, Paper No. 89-GT-240, pp. V002T03A009; 10 pages.
- Bonnington, S. T. and A. L. King (1972). *Jet Pumps and Ejectors-A State of the Art Review and Bibliography*. British Hydromechanics Research Association, Fluid Engineering.
- Carletti, M. J., C. B. Rogers, and D. E. Parekh (1995). Use of streamwise vorticity to increase mass entrainment in a cylindrical ejector. *AIAA Journal* 33(9), 1641–1645.
- Chen, Q. (2008). *Performance of air-air ejectors with multi-ring entraining diffusers*. Ph. D. thesis, Department of Mechanical and Materials Engineering, Queen's University.
- Chen, Q. and A. M. Birk (2009). Experimental study of oblong exhaust ejector with multiring oblong entraining diffusers. *Journal of Engineering for Gas Turbines and Power* 131, 062302.
- Fox, R. and A. McDonald (1971). Effects of swirling inlet flow on pressure recovery in conical diffusers. *AIAA Journal* 9(10), 2014–2018.
- Hoffmann, J. and G. Gonzalez (1984). Effects of small-scale, high intensity inlet turbulence on flow in a two-dimensional diffuser. *Journal of flu-ids engineering* 106(2), 121–124.
- Hu, H., S. Wu, G. Shen, and E. L. Yagoda (1996). Effect of tabs on the vortical and turbulent structures of jet flows. *ASME-Publications-Fed* 237, 77–84.
- Hu, H., T. Saga, T. Kobayashi, and N. Taniguchi (2000). Research on the vortical and turbulent structures in the lobed jet flow using laser induced fluorescence and particle image velocime-try techniques. *Measurement Science and Technology* 11(6), 698.
- Kastner, L. J. and J. R. Spooner (1950). An investigation of the performance and design of the air ejector employing low-pressure air as the driving fluid. *Proceedings of the Institution of Mechanical Engineers* 162(1), 149–166.
- Klein, A. (1981). Review: Effects of inlet conditions on conical-diffuser performance. *Journal of Flu-ids Engineering* 103(2), 250–257.
- Launder, B. E. and D. Spalding (1974). The numerical computation of turbulent flows.

- Computer Methods in Applied Mechanics and Engineering* 3(2), 269–289.
- Mahulikar, S. P., H. R. Sonawane, and G. A. Rao (2007). Infrared signature studies of aerospace vehicles. *Progress in Aerospace Sciences* 43(7), 218–245.
- Manganiello, E. J. and D. Bogatsky (1976). An experimental investigation of rectangular exhaust gas ejectors applicable for engine cooling. Report NACA-TR-818, 161–179.
- Menter, F. R. (1994). Two-equation eddy-viscosity turbulence models for engineering applications. *AIAA Journal* 32(8), 1598–1605.
- Mitchell, J. W. and A. L. London (1958). Design parameters for subsonic air-air ejectors. Stanford University, Department of Mechanical Engineering, Technical Report 40.
- Mohammadaliha, N., H. Afshin, and B. Farahanieh (2016). Numerical investigation of nozzle geometry effect on turbulent 3-d water offset jet flows. *Journal of Applied Fluid Mechanics* 9(4).
- Mueller, N. (1964). Water jet pump. *Journal of the Hydraulics Division* 90(3), 83–113.
- Nicoll, W. B. and B. R. Ramaprian (1970). Performance of conical diffusers with annular injection at inlet. *Journal of Fluids Engineering* 92(4), 827–835.
- Quinn, B. (1959). Ejector performance at high temperatures and pressures. *Journal of Aircraft* 13(12), 948–954.
- Henry, R., C. C. W. and S. W. Wilbur (1956). Summary of subsonic-diffuser data. NACA RM L56F05.
- Rao, G. A. and S. P. Mahulikar (2002). Integrated review of stealth technology and its role in airpower. *The Aeronautical Journal* 106(1066), 629642.
- Reddy, Y. and S. Kar (1968). Theory and performance of water jet pump. *Journal of the Hydraulics Division* 94(5), 1261–1282.
- Reneau, L. R., J. P. Johnston, and S. J. Kline (1967, mar). Performance and Design of Straight, Two-Dimensional Diffusers. *Journal of Basic Engineering* 89(1), 141–150.
- Ricou, F. P. and D. Spalding (1961). Measurements of entrainment by axisymmetrical turbulent jets. *Journal of fluid mechanics* 11(01), 21–32.
- Sen, S. (2008). *Studies on Flow Characteristics of a Stepped Conical Diffuser with Passive Suction*. Ph. D. thesis, Department of Applied Mechanics, Indian Institute of Technology Delhi.
- Senoo, Y., N. Kawaguchi, and T. Nagata (1978). Swirl flow in conical diffusers. *Bulletin of JSME* 21(151), 112–119.
- Shih, T.-H., W. W. Liou, A. Shabbir, Z. Yang, and J. Zhu (1995). A new k- ϵ eddy viscosity model for high Reynolds number turbulent flows. *Computers & Fluids* 24(3), 227–238.
- Silvester, R. and N. H. Mueller (1968). Design data for the liquid-liquid jet pump. *Journal of Hydraulic Research* 6(2), 129–162.
- Singh, L., Singh, S., & Sinha, S. (2018). Effect of standoff distance and area ratio on the performance of circular exhaust ejector using computational fluid dynamics. Proceedings of the Institution of Mechanical Engineers, Part G: *Journal of Aerospace Engineering* 232(15), 2821–2832.
- Singh, P., S. N. Singh, and V. Seshadri (2009). Experimental Investigations on Non-Circular Ejector Air Diffusers. *39th AIAA Fluid Dynamics Conference*, 4213.
- Singh, P., S. N. Singh, and V. Seshadri (2013). Effect of number of slots and overlap on the performance of non-circular ejector air diffuser. In *43rd AIAA Fluid Dynamics Conference*, 2729.
- Singh, P., S. Singh, and V. Seshadri (2016). Studies on stepped air ejector diffusers incorporating heat transfer effects. *International Journal of Turbo & Jet-Engines* 35(3), 251–263.
- Skebe, S., D. McCormick, and W. Presz, JR. (1988, jan). Parameter effects on mixer-ejector pumping performance. In *26th Aerospace Sciences Meeting*, Reston, Virginia. American Institute of Aeronautics and Astronautics.
- Toulmay, F. (1988). Internal aerodynamics of infrared suppressors for helicopter engines. *Journal of the American Helicopter Society* 33(4), 4–14.
- Vyas, B. and S. Kar (1975). Study of entrainment and mixing process for an air to air jet ejector. In *Second Symposium on Jet Pumps and Ejectors and Gas Lift Techniques*, BHRA Fluid Engineering, pp. C2-15-C2-25, Volume 1, 2.
- Waitman, B. A., L. R. Reneau, and S. J. Kline (1961). Effect of inlet conditions on performance of two dimensional subsonic diffusers. *Journal of Basic Engineering, Transaction of ASME* 83(3), 349–360.